ChemComm

COMMUNICATION

View Article Online
View Journal | View Issue

Check for updates

Cite this: *Chem. Commun.*, 2024, **60**, 13578

Received 15th September 2024,
Accepted 23rd October 2024

DOI: 10.1039/d4cc04771k

rsc.li/chemcomm

Published on 24 October 2024. Downloaded on 6/3/2026 2:57:47 AM.

A highly conductive and antioxidative MoO_2-doped Li argyrodite electrolyte for all-solid-state Li batteries†

Yinglei Wu,*[a] Runze Zhang,[ab] Qianjin Huang,[ab] Jingjing Wang,[b] Kaiyue Jiang,[bd] Zhenying Chen,[bc] Jinhui Zhu *[b] and Xiaodong Zhuang *[bd]

A MoO_2-doped $Li_{5.5}PS_{4.5}Cl_{1.5}$ solid electrolyte with ionic conductivity of 12 mS cm^{-1} and an electrochemical window of 4.3 V *vs.* Li/Li$^+$ was prepared, which enables a $LiNi_{0.8}Co_{0.1}Mn_{0.1}O_2$-based full cell to deliver a specific capacity of 194 mA h g^{-1} at 0.1C and retain 80% capacity after 3500 cycles at 1C.

The rapid development of electric vehicles has aroused demand for high-energy-density, high-safety all-solid-state Li batteries (ASSLBs).[1] These batteries are designed by employing safer solid electrolytes (SEs) to replace hazardous liquid electrolytes and separators found in traditional Li-ion batteries.[2] As key components, SEs are categorized into polymer-, oxide-, sulfide-, and halide-based electrolytes.[3] Among these, sulfide-based SEs (SSEs) have garnered the most attention due to their particularly high ionic conductivity (σ_i) and favorable mechanical properties, such as high elasticity and ductility. These characteristics offer the potential to improve both the safety and the energy-power performance of ASSLBs.[4,5]

Of the various SSEs, Li argyrodite of Li_6PS_5Cl is the most widely used due to its high σ_i (>1 mS cm^{-1}), excellent ductility (low grain boundary resistance), and cost-effective raw materials that avoid rare elements.[6] However, Li_6PS_5Cl suffers from poor electrochemical stability and requires enhanced σ_i.[7] Substituting P, S, and Cl sites in Li_6PS_5Cl with other elements can modify the Li sublattice and increase S^{2-}/Cl^- site disorder, facilitating Li^+ diffusion and improving σ_i.[8,9] Additionally, doping elements such as In, Sn, Mg, F, and I can aid in the formation of a favorable solid electrolyte interphase (SEI), stabilizing the Li metal anode.[7,10–12] Despite these advances, little research has been dedicated to improving the oxidation stability of Li_6PS_5Cl for compatibility with uncoated high-voltage cathodes.

In this study, we introduce dual-functional MoO_2 into the crystal lattice of Cl-rich $Li_{5.5}PS_{4.5}Cl_{1.5}$ SSE by substituting a portion of P_2S_5 raw material with MoO_2 (1–3%). The optimized $Li_{5.51}P_{0.99}Mo_{0.01}S_{4.48}O_{0.02}Cl_{1.5}$ SSE exhibits higher σ_i (12.0 *vs.* 9.1 mS cm^{-1}) and a wider electrochemical stability window (4.3 *vs.* 3.1 V *vs.* Li/Li$^+$) compared to the $Li_{5.5}PS_{4.5}Cl_{1.5}$ matrix. As a result, a full cell using this modified SSE and an uncoated single-crystal $LiNi_{0.8}Co_{0.1}Mn_{0.1}O_2$ (NCM811) cathode achieves a high specific capacity (194 mA h g^{-1} at 0.1C) and an ultralong cycling life (80% capacity retention after 3500 cycles at 1C). *In situ* Raman spectroscopy and *ex situ* X-ray photoelectron spectroscopy (XPS) confirm the excellent oxidation resistance of the MoO_2-doped Li argyrodite.

A series of MoO_2-doped $Li_{5.5+x}P_{1-x}Mo_xS_{4.5-2x}O_{2x}Cl_{1.5}$ (x = 0.01, 0.02, 0.03) and control $Li_{5.5}PS_{4.5}Cl_{1.5}$ SSEs were synthesized through a solid-state process involving initial ball milling, followed by cold pressing, and finally annealing. The prepared $Li_{5.5+x}P_{1-x}Mo_xS_{4.5-2x}O_{2x}Cl_{1.5}$ SSEs exhibit an aggregation morphology with primary particle sizes ranging from a few microns to ten microns, with all elements distributed homogeneously. The MoO_2 doping does not alter the morphology and elemental distribution of the SSEs (Fig. S1–S5, ESI†). The crystalline structures of the synthesized SSEs were analyzed using X-ray diffraction (XRD). As shown in Fig. 1a, all samples exhibit similar XRD patterns that align with Li_7PS_6 (PDF#34-0688), indicating a cubic $F\bar{4}3m$ space group. As the MoO_2 content increases, impurity peaks from LiCl and Li_3PO_4 become more pronounced due to the limited solubility of Mo and O dopants. Additionally, the main peaks in the XRD patterns of $Li_{5.5+x}P_{1-x}Mo_xS_{4.5-2x}O_{2x}Cl_{1.5}$ shift slightly to smaller 2θ angles as the dopant concentration increases (Fig. 1b), indicating unit cell expansion.[10] This expansion can be attributed to the

[a] *School of Chemistry and Chemical Engineering, Shanghai University of Engineering Science, Shanghai 201620, China. E-mail: wuyl@sues.edu.cn*
[b] *The Soft2D Lab, State Key Laboratory of Metal Matrix Composites, Shanghai Key Laboratory of Electrical Insulation and Thermal Ageing, School of Chemistry and Chemical Engineering, Shanghai Jiao Tong University, Shanghai 200240, China. E-mail: zhujinhui1109@sjtu.edu.cn, zhuang@sjtu.edu.cn*
[c] *College of Chemistry, Zhengzhou University, Zhengzhou 450001, Henan, China*
[d] *Frontiers Science Center for Transformative Molecules, Zhang Jiang Institute for Advanced Study, Shanghai Jiao Tong University, Shanghai 201203, China*

† Electronic supplementary information (ESI) available. See DOI: https://doi.org/10.1039/d4cc04771k

This journal is © The Royal Society of Chemistry 2024

Published on 24 October 2024. Downloaded on 6/3/2026 2:57:47 AM.

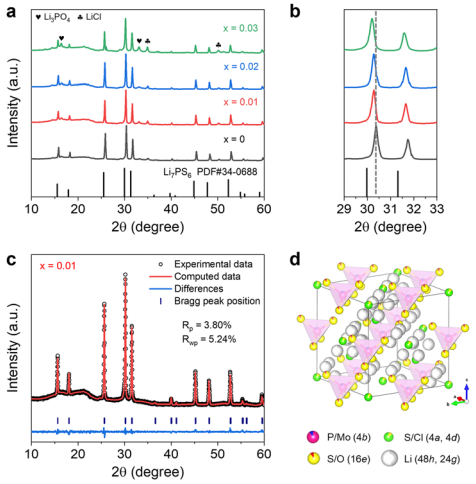

Fig. 1 (a) and (b) XRD patterns of $Li_{5.5+x}P_{1-x}Mo_xS_{4.5-2x}O_{2x}Cl_{1.5}$ (x = 0, 0.01, 0.02, 0.03). Rietveld XRD pattern refinement (c) and crystal structural diagram (d) of $Li_{5.51}P_{0.99}Mo_{0.01}S_{4.48}O_{0.02}Cl_{1.5}$.

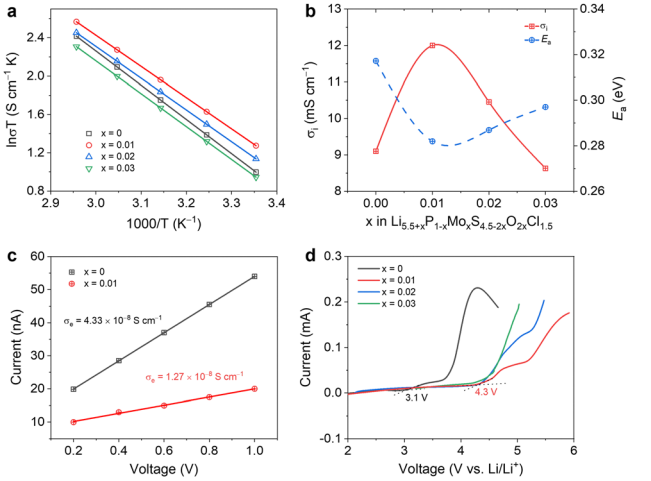

Fig. 2 Electrochemical properties of $Li_{5.5+x}P_{1-x}Mo_xS_{4.5-2x}O_{2x}Cl_{1.5}$ (x = 0, 0.01, 0.02, 0.03). (a) Arrhenius curves, (b) RT σ_i and E_a, (c) σ_e, and (d) ESWs.

substitution of smaller P^{5+} ions with larger Mo^{4+} ions (34 *vs.* 65 pm). The doping of lower-valence Mo^{4+} also increases the Li^+ concentration within the lattice, improving σ_i.[7]

To further evaluate the structural changes in the SSE following MoO_2 incorporation, Rietveld refinement of the XRD pattern of $Li_{5.51}P_{0.99}Mo_{0.01}S_{4.48}O_{0.02}Cl_{1.5}$ was performed (Fig. 1c and Table S1, ESI†). The calculated pattern matches the experimental data, confirming the successful doping of MoO_2, forming a cubic argyrodite-type $Li_{5.51}P_{0.99}Mo_{0.01}S_{4.48}O_{0.02}Cl_{1.5}$ SSE with the $F\bar{4}3m$ space group. Fig. 1d illustrates the crystalline structure of the MoO_2-doped SSE, where Mo atoms substitute P atoms at the 4b site, and O atoms replace S atoms at the 16e site.[10] Furthermore, the ^7Li magic angle spinning nuclear magnetic resonance spectra for both $Li_{5.51}P_{0.99}Mo_{0.01}S_{4.48}O_{0.02}Cl_{1.5}$ and $Li_{5.5}PS_{4.5}Cl_{1.5}$ show a single peak without a shift (Fig. S6, ESI†), indicating similar Li chemical environments in both samples. This further confirms the successful substitution of P and S atoms by Mo and O atoms, consistent with the XRD results.

The chemical composition of the synthesized $Li_{5.5+x}P_{1-x}Mo_xS_{4.5-2x}O_{2x}Cl_{1.5}$ (x = 0, 0.01) SSEs was examined using XPS. The P 2p XPS spectra (Fig. S7a, ESI†) show characteristic peaks for PS_4^{3-} at 131.8 and 132.7 eV in both samples.[13] Additionally, a peak at 133.7 eV corresponds to PO_4^{3-}, likely due to minor oxidation of PS_4^{3-}.[14] The S 2p (Fig. S7b, ESI†) and Mo 3d (Fig. S7c, ESI†) XPS spectra of the $Li_{5.51}P_{0.99}Mo_{0.01}S_{4.48}O_{0.02}Cl_{1.5}$ SSE confirm the presence of Mo–S bonds and the absence of Mo–O bonds,[15] further verifying successful doping of Mo and O atoms into the lattice, replacing P and S atoms, respectively. Raman spectra of all prepared SSEs show characteristic peaks for PS_4^{3-} at 198, 265, 428, 576, and 598 cm^{-1}.[16] Additionally, the Mo–S peak at 490 cm^{-1} is observed in the MoO_2-doped SSEs, with its intensity increasing as the MoO_2 content rises (Fig. S8, ESI†).[15]

The σ_i of the synthesized $Li_{5.5+x}P_{1-x}Mo_xS_{4.5-2x}O_{2x}Cl_{1.5}$ (x = 0, 0.01, 0.02, 0.03) SSEs was measured using electrochemical impedance spectroscopy (EIS). The resulting Nyquist plots and corresponding Arrhenius curves are displayed in Fig. S9 (ESI†) and Fig. 2a, respectively. Based on the calculations, the room temperature (RT, 25 °C) σ_i and activation energy (E_a) of all the SSEs were determined (Fig. 2b). The RT σ_i of the $Li_{5.5}PS_{4.5}Cl_{1.5}$ matrix is calculated to be 9.1 mS cm^{-1}, consistent with previously reported values.[17] Notably, doping with 1% MoO_2 significantly enhances the RT σ_i of the SSE to 12.0 mS cm^{-1}. To the best of our knowledge, this is the highest reported RT σ_i, surpassing those of previously reported O-doped Li argyrodites (Fig. S10 and Table S2, ESI†), as O doping typically has a negative impact on the σ_i of SSEs.[11] The enhanced RT σ_i of the $Li_{5.51}P_{0.99}Mo_{0.01}S_{4.48}O_{0.02}Cl_{1.5}$ SSE can be attributed to (i) the inherently high σ_i of the $Li_{5.5}PS_{4.5}Cl_{1.5}$ matrix, and (ii) moderate Mo doping, which increases Li^+ concentration and expands Li^+ transport pathways.[10] However, with higher MoO_2 doping levels, the detrimental effects of O doping become predominant, resulting in a decrease in RT σ_i. The E_a of the SSEs exhibits an inverse relationship with their RT σ_i, with the $Li_{5.51}P_{0.99}Mo_{0.01}S_{4.48}O_{0.02}Cl_{1.5}$ SSE showing the lowest E_a of 0.28 eV, indicating the fastest Li^+ transfer kinetics.

The electronic conductivity (σ_e) of SEs is typically used to assess their ability to suppress the growth of Li/Li-alloy dendrites.[7] As shown in Fig. S11 (ESI†) and Fig. 2c, the σ_e of the $Li_{5.51}P_{0.99}Mo_{0.01}S_{4.48}O_{0.02}Cl_{1.5}$ SSE is calculated to be 1.27 × 10^{-8} S cm^{-1}, which is significantly lower than that of the $Li_{5.5}PS_{4.5}Cl_{1.5}$ matrix (4.33 × 10^{-8} S cm^{-1}). This suggests that the MoO_2-doped SSE forms a more stable interface with Li/Li-alloy anodes, which also can be clarified in the Li|Li (Fig. S12, ESI†) and Li|Cu cells (Fig. S13, ESI†). The electrochemical stability window (ESW), which reflects the oxidative stability of SEs, was measured using linear sweep voltammetry (LSV). As shown in Fig. 2d, the MoO_2-doped SSEs exhibit a much wider ESW compared to $Li_{5.5}PS_{4.5}Cl_{1.5}$ SSE (4.3 *vs.* 3.1 V *vs.* Li/Li^+), indicating that the MoO_2-doped SSEs are more stable when paired with high-voltage Li-layered oxide cathodes.

The performance of the synthesized SSEs was further evaluated in Li–In|NCM811 full cells, where the SSEs functioned as both the separator and a component of the composite cathode.

Published on 24 October 2024. Downloaded on 6/3/2026 2:57:47 AM.

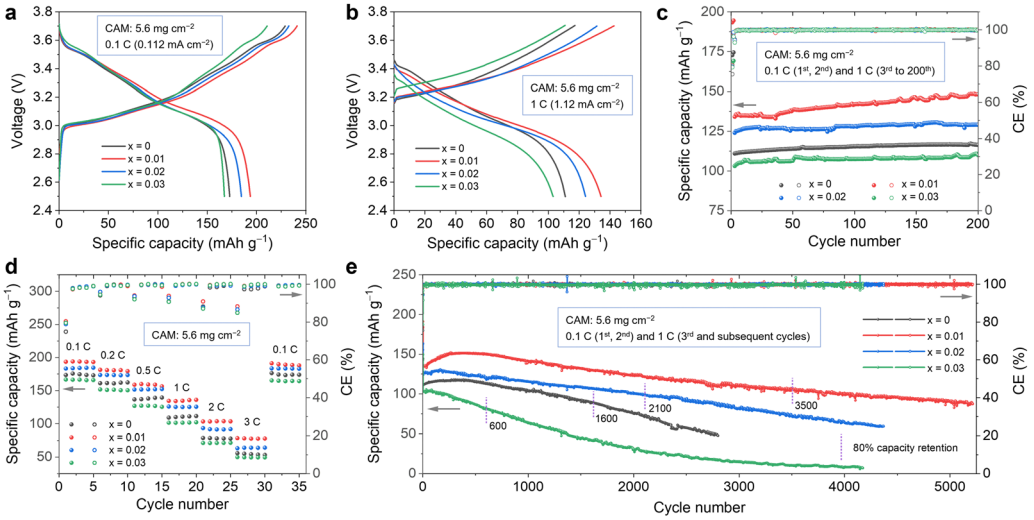

Fig. 3 Electrochemical performance of Li–In|NCM811 full cells with the as-prepared SSEs. (a) Voltage profiles at 0.1C, (b) voltage profiles at 1C, (c) performance comparison, (d) rate capability, and (e) long-term cycling stability.

All tests were conducted at RT under 35 MPa, with a cathode active material (CAM) loading of 5.6 mg cm^{-2}. Fig. 3a presents the initial voltage profiles of the full cells using the four different SSEs at 0.1C (1C = 200 mA g^{-1}). Notably, the cell using the $Li_{5.51}P_{0.99}Mo_{0.01}S_{4.48}O_{0.02}Cl_{1.5}$ SSE delivers the highest specific capacity of 194 mA h g^{-1} with a coulombic efficiency (CE) of 80.5%. In comparison, the cell with the $Li_{5.5}PS_{4.5}Cl_{1.5}$ SSE achieves an initial specific capacity of 173 mA h g^{-1} and a CE of 75.5%. At a higher rate of 1C, the cell with 1% MoO_2-doped SSE still exhibits the highest specific capacity of 134 mA h g^{-1} (Fig. 3b).

The long-term electrochemical performance of the cells with the four SSEs was further assessed through repeated galvanostatic charge–discharge cycling (Fig. 3c). All cells demonstrate high stability over 200 cycles. Among them, the cell with 1% MoO_2-doped SSE maintains the highest specific capacity, followed by the cell with 2% MoO_2-doped SSE. The undoped SSE-based cell comes next, while the cell with 3% MoO_2-doped SSE shows the lowest specific capacity. This suggests a positive correlation between the electrochemical performance of the full cells and the RT σ_i of the adopted SSEs.

The rate capability of the full cells with the synthesized SSEs was also evaluated (Fig. 3d and Fig. S14, ESI†). The cell with $Li_{5.51}P_{0.99}Mo_{0.01}S_{4.48}O_{0.02}Cl_{1.5}$ SSE demonstrates the best rate performance, achieving specific capacities of 194, 181, 160, 134, 103, and 78 mA h g^{-1} at rates of 0.1C, 0.2C, 0.5C, 1C, 2C, and 3C, respectively. Additionally, the specific capacity recovered when the rate returns to 0.1C. Long-term cycling stability was also compared for the full cells using the four SSEs. As shown in Fig. 3e, the cell with $Li_{5.51}P_{0.99}Mo_{0.01}S_{4.48}O_{0.02}Cl_{1.5}$ SSE operates for over 5000 cycles at 1C and maintains 80% capacity retention after 3500 cycles. In contrast, the cells with 2% MoO_2-doped, undoped, and 3% MoO_2-doped SSEs achieve 80% capacity retention after 2100, 1600, and 600 cycles, respectively. Overall, the full cell with 1% MoO_2-doped SSE exhibits significantly better electrochemical performance compared to previously reported O-doped Li argyrodite-based full cells (Table S3, ESI†).

To assess the interface evolution within the full cells, *in situ* EIS measurements were conducted on $Li_{5.51}P_{0.99}Mo_{0.01}S_{4.48}O_{0.02}Cl_{1.5}$ and $Li_{5.5}PS_{4.5}Cl_{1.5}$ SSE-based full cells during the initial charge–discharge cycles. Nyquist plots (Fig. S15a, ESI†) and the corresponding equivalent circuit fitting values (Table S4, ESI†) reveal that the cathodic interfacial resistance (R_{CI}) of the $Li_{5.51}P_{0.99}Mo_{0.01}S_{4.48}O_{0.02}Cl_{1.5}$ SSE-based cell increases from 20.8 to 108.7 Ω over the first cycle. In comparison, the $Li_{5.5}PS_{4.5}Cl_{1.5}$ SSE-based cell exhibits a larger initial R_{CI} of 70.4 Ω, which increases to 239.8 Ω after the first cycle (Fig. S16a, ESI†). These results demonstrate that the MoO_2-doped SSE provides better stability with NCM811 than the undoped SSE. To gain further insight, the distribution of the relaxation time (DRT) diagrams was transformed from the Nyquist plots, providing detailed impedance information. As shown in Fig. S15b, c and S16b, c (ESI†), the DRT spectra exhibit five distinct peaks corresponding to different resistances: grain boundary (10^{-6} s), SEI/cathode electrolyte interphase (CEI) (10^{-5} s), charge transfer at the anode and cathode (10^{-4}–10^{-3} and 10^{-2}–10^{-1} s), and solid-state diffusion (10^{0}–10^{1} s).[18] The results confirm that the R_{CI}, including CEI and cathodic charge transfer resistance, increases continuously during charging and discharging.

In situ Raman spectroscopy was employed to detect the compositional evolution of the cathodic interface during the first charge–discharge cycle. The Raman spectra collected at the $Li_{5.51}P_{0.99}Mo_{0.01}S_{4.48}O_{0.02}Cl_{1.5}$ SSE–NCM811 interface (Fig. 4a) show only the characteristic peaks of the PS_4^{3-} tetrahedron and the Mo–S bond.[16] Furthermore, the intensity of the PS_4^{3-} main peak at 428 cm^{-1} remains constant during cycling (Fig. S17a, ESI†), indicating the exceptional stability of the MoO_2-doped SSE under high voltage and oxidation conditions. In sharp contrast, the *in situ* Raman spectra for the $Li_{5.5}PS_{4.5}Cl_{1.5}$ SSE–NCM811 interface (Fig. 4b) show a distinct S–S bond peak at 472 cm^{-1} in addition to the PS_4^{3-} peaks.[19] Moreover, the intensity of the PS_4^{3-} peak decreases during

 This journal is © The Royal Society of Chemistry 2024

Published on 24 October 2024. Downloaded on 6/3/2026 2:57:47 AM.

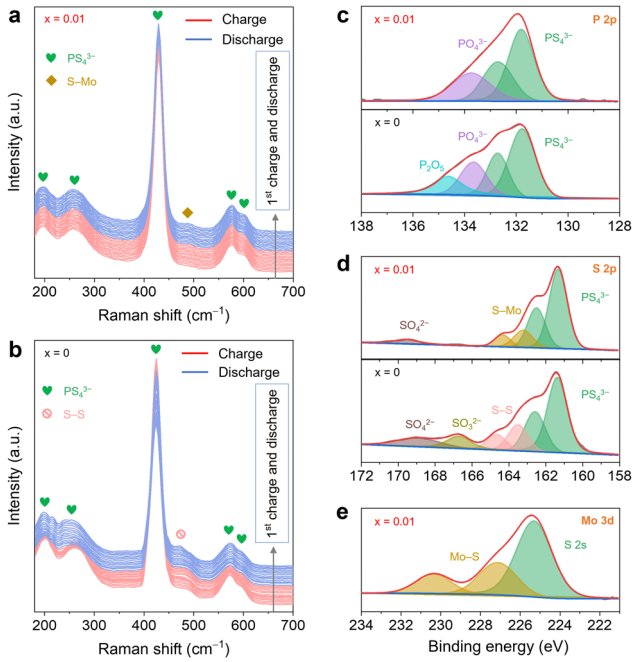

Fig. 4 *In situ* Raman spectra collected at the cathodic interface with (a) $Li_{5.51}P_{0.99}Mo_{0.01}S_{4.48}O_{0.02}Cl_{1.5}$, and (b) $Li_{5.5}PS_{4.5}Cl_{1.5}$ SSEs. P 2p (c), S 2p (d), and Mo 3d (e) XPS spectra of the cycled composite cathodes.

cycling (Fig. S17b, ESI†), suggesting that the undoped SSE is prone to oxidation, forming high-valence S species.

To further evaluate the antioxidative durability of the synthesized SSEs, full cells cycled for 200 cycles were disassembled, and the composite cathodes were analyzed. The cycled cathode with $Li_{5.51}P_{0.99}Mo_{0.01}S_{4.48}O_{0.02}Cl_{1.5}$ SSE retains an intact and dense morphology, whereas the cathode with $Li_{5.5}PS_{4.5}Cl_{1.5}$ SSE exhibits voids and cracks (Fig. S18, ESI†). The P 2p XPS spectrum of the cycled $Li_{5.51}P_{0.99}Mo_{0.01}S_{4.48}O_{0.02}Cl_{1.5}$ SSE (Fig. 4c and Table S5, ESI†) shows peaks corresponding to PS_4^{3-} and PO_4^{3-},[14] with the PO_4^{3-} content remaining close to that in the fresh SSE. In contrast, the cycled $Li_{5.5}PS_{4.5}Cl_{1.5}$ SSE exhibits an increased PO_4^{3-} content and the formation of a new oxidized product, P_2O_5 (at 134.6 eV).[14] The S 2p XPS spectrum of the cycled $Li_{5.51}P_{0.99}Mo_{0.01}S_{4.48}O_{0.02}Cl_{1.5}$ SSE (Fig. 4d and Table S5, ESI†) shows, in addition to the PS_4^{3-} and S–Mo bond, a small amount of sulfate (5.44%).[20] In contrast, around 40% of the $Li_{5.5}PS_{4.5}Cl_{1.5}$ SSE is oxidized to form S–S bonds (163.5 and 164.7 eV) and sulfates after prolonged cycling.[20] The Mo 3d XPS spectrum of the cycled $Li_{5.51}P_{0.99}Mo_{0.01}S_{4.48}O_{0.02}Cl_{1.5}$ SSE (Fig. 4e) further confirms the high stability of the Mo–S bond under high-voltage conditions. In conclusion, MoO_2 doping significantly enhances the antioxidative stability of Li argyrodite, improving their performance in high-voltage applications.

In summary, a series of MoO_2-doped Li argyrodites were successfully synthesized *via* the conventional solid-state reaction method. The optimized SSE, with 1% MoO_2 doping, exhibits a high RT σ_i of 12.0 mS cm^{-1} and a broad ESW of 4.3 V *vs.* Li/Li^+. These properties enable the corresponding Li–In|NCM811 full cell to achieve an impressive specific capacity of 194 mA h g^{-1} at 0.1C, along with an ultra-long cycling life, retaining 80% of its capacity after 3500 cycles at 1C. *In situ* EIS, *in situ* Raman, and *ex situ* XPS analyses further confirm that the MoO_2-doped Li argyrodite demonstrates superior resistance to oxidation compared to the undoped counterpart.

This work was financially supported by the National Natural Science Foundation of China (NSFC: 52173205).

Data availability

The data supporting this article have been included as part of the ESI.†

Conflicts of interest

There are no conflicts to declare.

Notes and references

1 X. Hu, Z. Zhang, X. Zhang, Y. Wang, X. Yang, X. Wang, H. A. Yehezkel, S. Langford, D. Zhou, B. Li, G. Wang and D. Aurbach, *Nat. Rev. Mater.*, 2024, **9**, 305–320.
2 X. Yang, Q. Yin, C. Wang, K. Doyle-Davis, X. Sun and X. Li, *Prog. Mater. Sci.*, 2023, **140**, 101193.
3 L. Jia, J. Zhu, X. Zhang, B. Guo, Y. Du and X. Zhuang, *Electrochem. Energy Rev.*, 2024, **7**, 12.
4 J. Wu, S. Liu, F. Han, X. Yao and C. Wang, *Adv. Mater.*, 2020, **32**, 2000751.
5 N. Zhang, Q. He, L. Zhang, J. Zhang, L. Huang and X. Yao, *Adv. Mater.*, 2024, **36**, 2408903.
6 L. Zhou, K.-H. Park, X. Sun, F. Lalère, T. Adermann, P. Hartmann and L. F. Nazar, *ACS Energy Lett.*, 2018, **4**, 265–270.
7 C. Liu, B. Chen, T. Zhang, J. Zhang, R. Wang, J. Zheng, Q. Mao and X. Liu, *Angew. Chem., Int. Ed.*, 2023, **62**, e202302655.
8 S. Li, J. Lin, M. Schaller, S. Indris, X. Zhang, T. Brezesinski, C. W. Nan, S. Wang and F. Strauss, *Angew. Chem., Int. Ed.*, 2023, **62**, e202314155.
9 Y. Ma, Z. Yang and G. Zhang, *Acta Chim. Sin.*, 2023, **81**, 1387–1393.
10 C. Wang, J. Hao, J. Wu, H. Shi, L. Fan, J. Wang, Z. Wang, Z. Wang, L. Yang, Y. Gao, X. Yan and Y. Gu, *Adv. Funct. Mater.*, 2024, **34**, 2313308.
11 G. Li, S. Wu, H. Zheng, Y. Yang, J. Cai, H. Zhu, X. Huang, H. Liu and H. Duan, *Adv. Funct. Mater.*, 2022, **32**, 2211805.
12 G. Liu, J. Zhang, J. Yang, J. Chen, X. Xiao and X. Yao, *J. Energy Chem.*, 2025, **100**, 50–58.
13 X. Zhang, X. Li, S. Weng, S. Wu, Q. Liu, M. Cao, Y. Li, Z. Wang, L. Zhu, R. Xiao, D. Su, X. Yu, H. Li, L. Chen, Z. Wang and X. Wang, *Energy Environ. Sci.*, 2023, **16**, 1091–1099.
14 J. H. Zhu, J. Y. Luo, J. Y. Li, S. H. Huang, H. Z. Geng, Z. Y. Chen, L. N. Jia, Y. Z. Fu, X. Zhang and X. D. Zhuang, *Adv. Mater.*, 2024, **36**, e2407128.
15 R. Luo, W. W. Xu, Y. Zhang, Z. Wang, X. Wang, Y. Gao, P. Liu and M. Chen, *Nat. Commun.*, 2020, **11**, 1011.
16 R. Zhang, Y. Wu, Z. Chen, Y. Wang, J. Zhu and X. Zhuang, *J. Mater. Chem. A*, 2023, **11**, 19195–19209.
17 W. D. Jung, J.-S. Kim, S. Choi, S. Kim, M. Jeon, H.-G. Jung, K. Y. Chung, J.-H. Lee, B.-K. Kim, J.-H. Lee and H. Kim, *Nano Lett.*, 2020, **20**, 2303–2309.
18 Y. Lu, C.-Z. Zhao, J.-Q. Huang and Q. Zhang, *Joule*, 2022, **6**, 1172–1198.
19 D. Cao, X. Sun, F. Li, S. M. Bak, T. Ji, M. Geiwitz, K. S. Burch, Y. Du, G. Yang and H. Zhu, *Angew. Chem., Int. Ed.*, 2023, **62**, e202302363.
20 D. H. S. Tan, E. A. Wu, H. Nguyen, Z. Chen, M. A. T. Marple, J.-M. Doux, X. Wang, H. Yang, A. Banerjee and Y. S. Meng, *ACS Energy Lett.*, 2019, **4**, 2418–2427.